MRS Communications (2014), *4*, 113–119
© Materials Research Society, 2014
doi:10.1557/mrc.2014.23

MRS Communications

Research Letters

Crystallographic controlled dissolution and surface faceting in disordered face-centered cubic FePd

D. J. Horton, A. W. Zhu and **J. R. Scully,** Department of Materials Science and Engineering, Center for Electrochemical Science and Engineering, University of Virginia, Charlottesville, Virginia 22904
M. Neurock, Department of Chemical Engineering, University of Virginia, Charlottesville, Virginia 22904
Address all correspondence to D. J. Horton at **dh7h@virginia.edu**

(Received 28 July 2014; accepted 2 September 2014)

Abstract

Electrochemical dissolution by congruent oxidation of Fe Pd in 1 M HCl solution was strongly controlled by crystallographic orientation. Anodic dissolution was characterized over a wide variety of grain surface plane orientations providing a detailed view of the crystallographic nature of oxidative dissolution and surface facet evolution as a function of grain orientation. Near {100}-oriented grains retained low surface roughness after corrosion and low dissolution rates. Grains with orientation within 2° of {111} were also topographically smooth after dissolution and were nearly as corrosion resistant as {100} grains. Overall dissolution depth depended linearly on crystallographic angle within 40° of {100} and within 10° of {111} planes. Post-corrosion surface faceting and dissolution were substantially increased at grain orientations near {110} and were highest between 10° and 20° from the {111} plane normal. Grains at these crystallographic angles roughened during oxidative dissolution by forming complex semi-periodic topographies. These finely spaced arrays of terraces and ledges likely consisted of combinations of more corrosion resistant low-index planes. Therefore, the overall corrosion depth within a grain possessing an initially irrational crystal orientation was determined by the amount of dissolution required to expose new, slowly dissolving surface facets with low-index orientations. Computations of Fe–Pd alloy surface energies and surface atom coordination as a function of crystal orientation are utilized to help support this explanation.

Introduction

Many forms of electrochemical dissolution and deposition exhibit a rate dependence that depends on crystallographic orientation, but the governing structural factors are not well understood. The difference in corrosion behavior dependent on crystallographic orientations enabled fundamental explorations of the role of atomistic bonding, surface energy, surface relaxation and reconstruction, and other structural factors on electrochemically controlled dissolution[1–5] and also the metal–oxide–solution epitaxy interface during passivation and pitting corrosion.[6–10] True understanding of crystallographic behavior has broad implications toward the design of fine-scale surface structures by electrodissolution-based crystal and atomic-scale surface reorganization.

There exist significant discrepancies regarding which orientations result in the least corrosion resistance, to either dissolution or pitting.[2–4,11] Older studies relied on single crystals[4,6,9,10] and a relatively limited number of orientations.[1–3,7,8,11,12] A scanning droplet cell was used to survey dissolution activity prior to passivity for 30 well-distributed orientations in ferritic steel, but the underlying effect of structure is clouded by enrichment of the passivating species.[13] To date, no complete experimental dissolution study of a wide range and high number of face-centered cubic (fcc) orientations including orientations near the three low-index orientations in the absence of enrichment and redeposition has been presented. Most studies neglect solid solution alloys and are complicated by inclusions and intergranular corrosion due to segregation and/or oxides, which are often amorphous muting the effect of the underlying crystal structure. These practical limitations have led to unclear and often contradictory findings. Modern computational calculations of surface energy and fractions of surface atoms of various orientations, metallurgical "crystal mapping" and corrosion surface "scanning" methods in combination can provide new insights regarding this phenomenon.

Results are presented on active electrochemical dissolution of disordered fcc FePd. Dissolution of a binary solid solution alloy in a strong acid at high potential benefits from the absence of oxides, inclusions, precipitates, segregation effects, and secondary phases found in many engineering alloys and enables a fundamental investigation into the role of the surface structural orientation on active electrochemical dissolution. The depth of dissolution and resulting surface faceting was characterized for 300 individual grains. Subsequently, results are correlated to the exposed surface grain orientation, associated computationally determined surface energies and surface coordination.

https://doi.org/10.1557/mrc.2014.23 Published online by Cambridge University Press

Methods

The equiatomic Fe–Pd alloy was produced by the arc-melting technique using high purity 99.999% Fe and 99.9999% Pd under an argon atmosphere and homogenized at 1100 °C for 24 h. Recrystallization was performed at 950 °C for 10 h followed by water quench.

Grain orientations were determined prior to electrochemical investigations using a scanning electron microscope, JEOL 840a SEM with LAB_6 filament, equipped with an electron backscatter detector (EBSD). The average orientation for each grain was used to determine the Miller indices, $\{hkl\}$, of the exposed surface plane tested electrochemically. Each $\{hkl\}$ is defined in terms of β_i, the angle measured from a primary low-index cubic plane normal to the $\{hkl\}$ of interest and α_i the angle between β_i and either the line from $\{100\}$ to $\{110\}$ or from $\{100\}$ to $\{111\}$. $\beta_{\{100\}}$ is equivalent to the Euler angle Φ from the Bunge convention.[14] To determine the relative amounts of dissolution of different grain orientations and their arithmetic mean deviation surface roughness a confocal laser scanning microscope (CLSM, Zeiss LSM 510, vertical step size 0.1 μm) was used to create a topographical map of the EBSD characterized polycrystalline surfaces. Prior to electrochemical experiments, the as-polished, using 0.05 μm diamond slurry, surface roughness was 0.030 μm.

Electrochemical measurements were conducted using a traditional three-electrode setup with an exposed electrically isolated working electrode consisting of the fcc FePd samples with a saturated calomel reference electrode and platinum mesh counter electrode. Potential controlled dissolution experiments were performed at $0.45V_{SCE}$ above the dissolution potential for Pd/Pd^{2+} (to $PdCl_4^{2-}$), where there is no passivity and no significant surface redeposition or enrichment of Pd occurs.

Modeling

A first-principles total-energy calculation was performed using the Vienna *ab initio* simulation program (VASP)[15] with revised Perdew–Burke–Ernzerhof functionals. The basis-set cutoffs were set to "high accuracy" and *k*-point meshes were set using "Monkhorst–Pack" or Γ-centered settings. The procedure of calculating surface energy of the Fe–Pd-disordered FCC-A1 structure involved two steps:

1. To identify the lattice constant of the FCC-A1 structures of FePd, Fe and Pd atoms were assigned at different atomic sites at random through geometric optimization with the bulk energy E_{bulk} (per atom).
2. A slab of two surface units ($U \times V$) normal to a designated orientation (hkl) of the FCC-A1 structure of the optimized lattice constant was constructed and consisted of a number n (36–44) of atoms. The total energy was calculated with the surface exposed to vacuum of thickness 10–16 Å. Although one side of the surface was fixed, up to six surface layers of atoms on the other surface was either fixed or allowed to relax. The energies of the slabs for both situations, denoted as $E_{unrelaxed}$ and $E_{relaxed}$ were calculated with *k*-points meshes of $4 \times 4 \times 1$.

The surface energy γ can then be calculated according to the following formula:

$$\gamma = \frac{(E_{relaxed} - nE_{bulk}) - 0.5(E_{unrelax} - nE_{bulk})}{A}, \quad (1)$$

where A is the surface area of the slab. The first parenthetical calculates the energy to separate the bulk system into a relaxed surface, whereas the second subtracts one side of the slab that is referenced to the bulk. Typically, the values converged at different vacuum thicknesses and number of surface atom layers, depending on the orientation of each surface cleaved. The converged condition was identified for each of those structures. The means of the values were obtained among those four to nine structures. Standard deviations were typically are about 0.05–0.15 J/m^2 (3–9 $meV/Å^2$).

Results

Relationship between dissolution depth and crystallographic orientation

The dissolution depth of a given grain correlated with the orientation in the surface normal direction. A typical EBSD and CLSM characterized region is shown in Figs. 1(a)–1(c). The total accumulated anodic charge averaged over all exposed orientations during potentiostatic polarization for 400 s in 1 M HCl solution was 3.29 C/cm^2. In the CLSM topographical map, the red regions correspond to the highest, or least corroded, grains; whereas the blue-purple colored grains indicate those that experienced the greatest depth of dissolution. There is a clear and significant crystallographic dependence of dissolution and no preferential dissolution at the grain boundaries. The corresponding grain orientations for the CLSM characterized region are shown on a reduced inverse pole figure (IPF) in Fig. 1(b). The near $\{100\}$ orientations, red on the IPF, show the lowest quantitative depth of dissolution. Orientations near $\{111\}$ such as grain 6 show a decrease in surface roughness and decrease in dissolution compared to orientations slightly further away from the $\{111\}$. Low-index orientations in general not only had the least corrosion depth, but also had lower roughness at the sub-micrometer scale [Fig. 1(c)]. In contrast, grain 2 and other orientations between 10° and 20° from the $\{111\}$ pole, purple-blue on the EBSD map, show the highest corrosion susceptibility expressed as depth and the highest micrometer scale roughening. Grains with orientation near $\{110\}$ do not show as much decrease in corrosion susceptibility that accompanies grains with orientations near the $\{100\}$, extending to large angles from the plane normal, as well as near the $\{111\}$, extending to only very small angles.

The differences in the microscopic surface roughness of different grains are apparent in both the CLSM image and the SEM micrographs. An example of the morphological distinction between grains is shown in the SEM micrographs in Fig. 1(c). The morphologically smooth grains, 1 and 7,

https://doi.org/10.1557/mrc.2014.23 Published online by Cambridge University Press

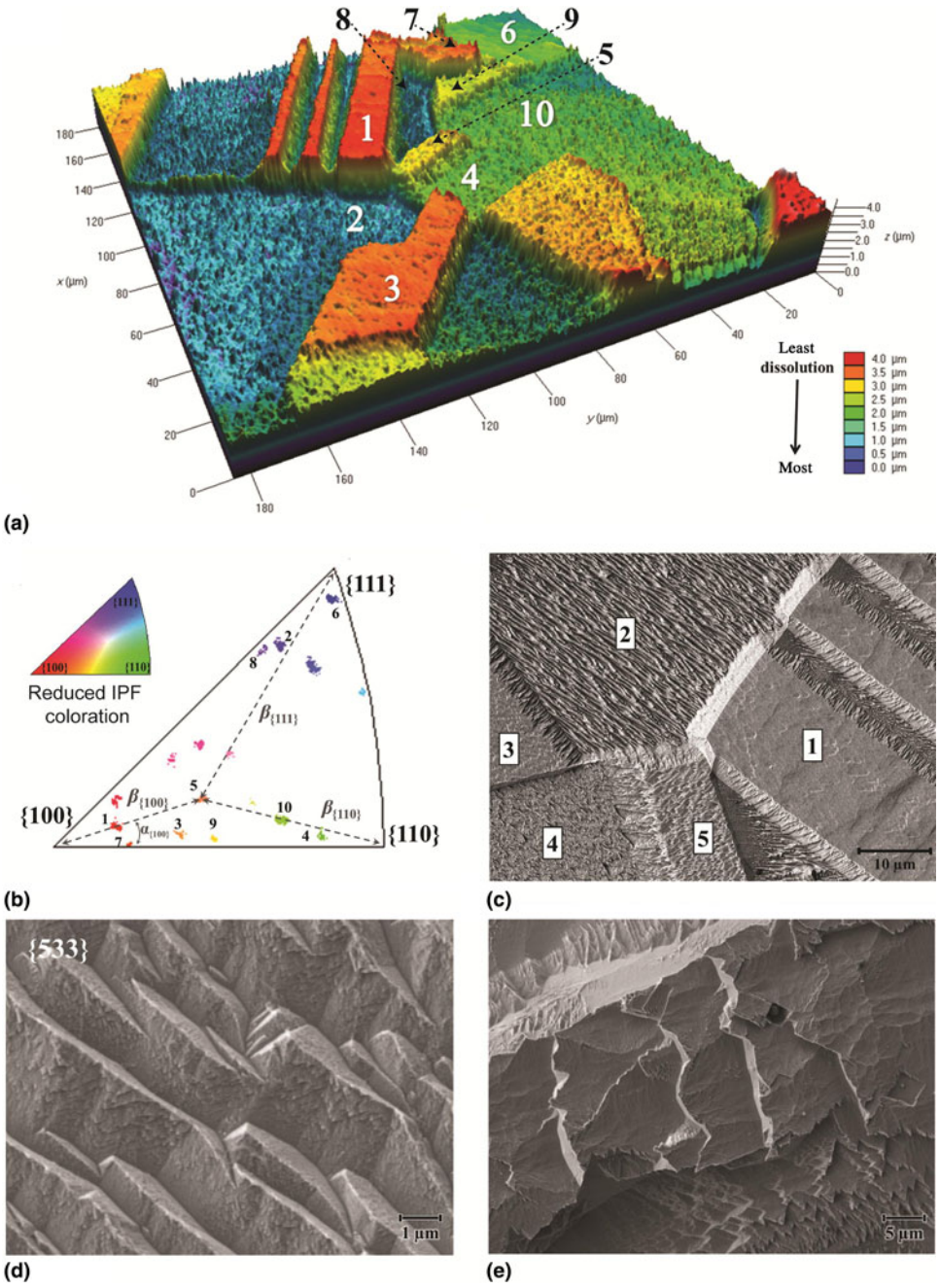


Figure 1. (a–c) CLSM, IPF, and SEM micrographs of a characterized region with 1.2 μm of average dissolution. (d) SEM micrograph of a {533} orientation, $\beta_{\{111\}} = 16°$ and (e) a grain with {100} facets after 3.8 and 15.7 μm of average dissolution, respectively.

correspond to regions near {100} with limited dissolution. Grain 6, $\beta\{111\} = 7°$, had significantly more dissolution than grains near the {100}. In contrast, grain 2 with an orientation of {533} and $\beta\{111\} = 13°$ had significantly increased dissolution and has distinct crystallographic surface faceting. Grains with orientations within 2° of the {110} plane normal had faceting with a surface roughness of 0.18 μm, twice the value of smooth grains. Grains 1, 3, and 6 are near either the {100} or {111} and have a surface that appears smooth and have a corresponding surface roughness of <0.09 μm. The most heavily dissolved grains, such as grains 2 and 8, also have the highest surface roughness, 0.25 μm.

After longer polarization times and increased dissolution, the surface morphology retains the crystallographic faceted structure characteristic of each grain. Grains near {100} and {111} show the characteristic scalloped morphology with no

https://doi.org/10.1557/mrc.2014.23 Published online by Cambridge University Press

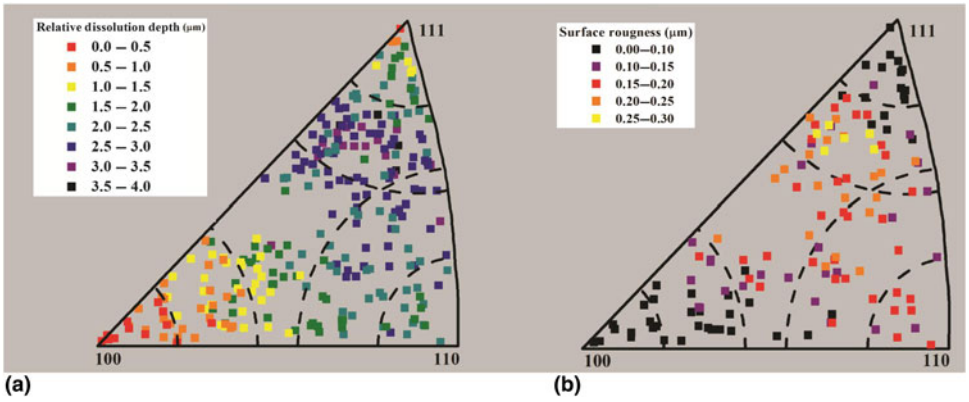


Figure 2. (a) Relative depth of dissolution and (b) Calculated surface roughness of grains as a function of orientation on an IPF in the surface normal direction. Dashed semicircles indicate 10° increments from the low-index orientations.

apparent crystallographic dependence. Figure 1(d) shows a grain with a {533} orientation, $\beta\{111\} = 16°$, which is one of the most highly dissolving orientations after 10.8 C/cm^2 of average current. This surface shows a highly faceted surface morphology consisting of a series of crystallographic terraces and steps. These features are more apparent after increased dissolution. Figure 1(e) depicts a grain with clear {100} faceting after an eightfold increase in dissolution depth. Figure 2 shows the corrosion susceptibility expressed as depth of penetration as well as the surface roughness for all 300 orientations measured yielding a more comprehensive picture than obtained previously as a function of orientation on IPFs. As the SEM micrographs and the CLSM topography indicate, the grains with the highest faceting are the grains with the greatest dissolution depth.

Figure 3 shows the dissolution depth as a function of $\beta\{100\}$. The dissolution depth increases as a linear function of angle. A linear fit of the data over the first 40°, excluding data within 10° of either {110} or {111}, has a slope of −0.071 μm/°, with a root-mean square (RMS) error of 0.33. The most susceptible region is between 35° and 45° from the {100}. For orientations near the {110}, indicated by the circles, the corrosion depth remains high. For $\beta\{111\} < 10°$, the depth of dissolution increases linearly with a slope of −0.24 μm/°, RMS error of 1.56, as the surface orientation tilt with respect to {111} increases, which is four times higher than the similar plot for $\beta\{100\}$. The corrosion rate at $\beta\{110\} < 20°$ does not show a statistically significant trend.

Model validation and surface energy calculations

The surface energy was determined using the VASP method for fcc Pd and fcc Fe. In the case of fcc Fe, the VASP calculations for {100}, {110}, and {111} are 2.10, 2.09, and 1.93 J/m^2, respectively. MEAM calculations for the same orientations are 2.08, 1.96, and 1.81.[16] The energy values for Pd are compared in Fig. 3 calculated using the VASP method (▲) and the MEAM method (circles,[17]). The ordinal ranking of the surface energy for these orientations for these different modeling methods is the same and the relative difference between orientations is similar. The surface energy FePd calculations for nine orientations, each an average of between four and nine randomly alloyed surfaces, ranged from a minimum at {100} and {111} at 1.83 to a maximum at {113} at 1.95 J/m^2. The normalized

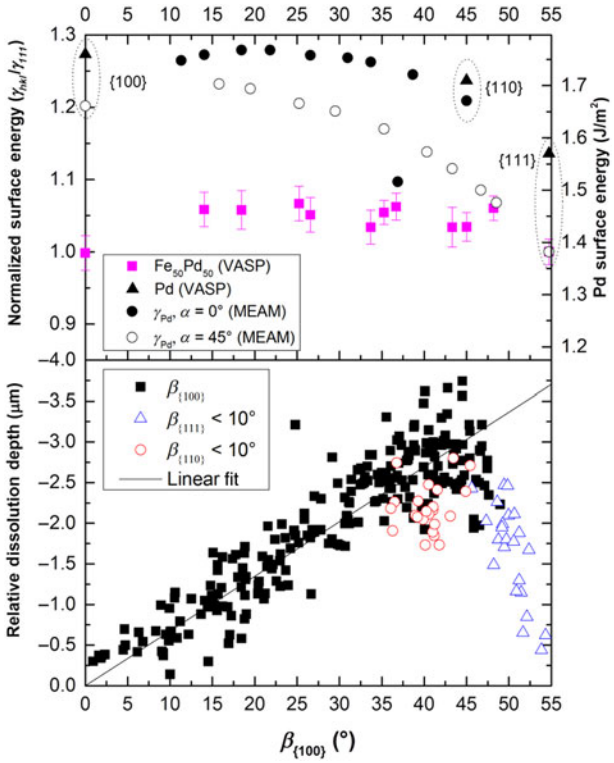


Figure 3. Relative depth of dissolution and normalized surface energy of FePd (VASP) and Pd (MEAM) as a function of $\beta_{\{100\}}$. For comparison, Pd (VASP) is compared to Pd (MEAM), right axis.

https://doi.org/10.1557/mrc.2014.23 Published online by Cambridge University Press

surface energy of FePd as a function of $\beta\{100\}$ is shown in Fig. 3 and compared to fcc Pd.[17]

Discussion

A peak in the dissolution at intermediate orientations has not yet been reported besides the present report. However, a peak number of pitting events on body-centered cubic (bcc) stainless steel in NaCl was observed around $\beta\{100\}$ of 25°.[8] In dissolution studies on polycrystalline fcc Al and Al alloys, the near {111} orientation typically showed the most dissolution of all orientations in NaOH solution.[2,3,11] Dissolution of the fast dissolving near {111} orientations revealed {111} terraces,[3,11] and then the {111} orientation showed a decreased dissolution rate. This is because fast {111} dissolution would reveal other slower dissolving facets and these facets would then form the terrace–ledge structure that would subsequently change more slowly. In bcc Fe, the {100} orientation is the least densely packed and typically shows the highest dissolution rate in H_2SO_4 solution[1] and NO_3^- solution.[18]

As mentioned in the Results section, a linear dependence of dissolution depth on $\beta\{100\}$ and $\beta\{111\}$ (Fig. 3) was observed. A linear dependence of corrosion on crystal orientation on β has been reported previously in several alloys, solution environments, and corrosion regimes. Konig and Davepon[12] studied oxidation of Ti in H_2SO_4 solution for about 20 different grain orientations by measuring the oxide interference patterns and a linear dependence of oxide thickness on β was observed. Grains near the (0001) basal plane had a thinner oxide and higher oxygen evolution current density. Schreiber et al.[7] measured the current of the first oxidation peak on Fe for 11 orientations in acetate buffer at pH 6 and found a linearly increasing current with respect to β from the {100} to the {111} plane normal. No dependence on α was observed. Holme et al.[2] measured Zn-induced alkaline etching dissolution depth in a predominantly Al alloy. The {111} orientation showed that the most dissolution and dissolution depth decreased linearly with $\beta\{111\}$. The underlying material factors responsible for these observations are still unclear. Several possibilities will be considered.

Surface energy considerations

It is reasonable to expect that dissolution occurs more readily from grains with higher surface energy where there are more low coordination surface atoms (CN) per unit area. In accordance with the atomistics of metal dissolution from kink sites or other exposed atoms, calculations of the surface energy by Nicholas[19,20] were made by taking into account the number of broken bonds of each atom on an ideal fcc crystal surface assuming no surface relaxation. Thus, orientations with a high number of broken bonds per unit area would have the highest surface energy. Metal oxidative dissolution is well known to occur from kink sites or exposed atoms where the activation energy to dissolution is likely at a minimum.[21] It is important to consider surface relaxation and reconstruction phenomena since their contributions to experimental observations can be significant because the surface CN can vary from unrelaxed surfaces due to these phenomena.[22] This study considered this. For instance VASP calculations of nearest neighbors show that $\beta\{100\}$ angles of 26.6 {210}, 18.4 {310}, 15.8 {511}, 32.3 {531}, and 51.3 {443} had CN as low as 6 or 7 over a considerable fraction of the surface. The {110} also had a CN of 7 on 50% of the surface atoms, whereas {100} and {111} had no surface atoms with CN below 8 and 9, respectively.

Refinements to these surface energy calculations accounted for broken bonds up to many next-nearest neighbor interactions. Recently, modeling techniques have been applied to calculate the surface energy of fcc materials in a similar manner as used here. Zhang et al.[17] calculated the surface energy of a series of fcc surfaces for 15 metals using a modified embedded atom approach, MEAM. For all the metals modeled including Pd, the densely packed {111} plane had the minimum surface energy. On average the {110} orientation was 22% higher and the {100} orientation was 20% higher compared to the minimum surface energy of the {111} plane.

Several key observations can be made based on the surface energy calculations for disordered FePd compared to other fcc metals. The difference between {100} and {111} is minimal (Fig. 3) which is in excellent agreement with the observed behavior of adjacent very near {100} and {111} orientations. The calculated FePd surface energy was higher at irrational planes and intermediate β values. No statistically significant dependence of surface energy on α is seen, unlike the sizable difference typically reported for the fcc metals, e.g., Pd (Fig. 3). Zhang's calculations show that the maximum calculated surface energy for FCC materials was typically at $\alpha = 0$, i.e., orientations between the {100} and {110} plane normals on the IPF, e.g., {210}, {310}, and {520}. No dissolution dependence on α was observed in our energy calculations or our results (Fig. 2). A strong dependence on $\beta\{100\}$ and $\beta\{111\}$ is seen in the corrosion behavior and follows the trend in surface energy.

In agreement with our findings, Heyraud and Metois[23] measured the equilibrium shape of fcc Pb at a series of temperatures and found that the {111} orientation had the lowest surface energy while the {100} and {110} orientations were approximately 2 and 5% higher, respectively. Moreover, the slope of surface energy increased with crystal angle from the {100} orientation more gradually than from the {111} orientation, while there is little to no decrease near the {110} orientation. These features are even more pronounced in similar measurements of the surface energy of Cu by McLean.[24] The surface energy increased very gradually up to 40° from the {100} orientation then decreases sharply to the minima at {111}. Similarly, no decrease is measured in proximity to the {110} zone; see Fig. 2. Additionally, the maximum surface energy is within 20° of the {111}-axis. The slopes of these lines are somewhat similar to those observed in Fig. 3. The minimum surface energy is still the close packed {111} plane. The measured regions of maximum dissolution were between 10° and 20° from the {111} plane normal in this study (Fig. 3), which

https://doi.org/10.1557/mrc.2014.23 Published online by Cambridge University Press

is in excellent agreement with these studies. Moreover, upon consideration of the behavior at the individual atom level, additional differences can be discerned that were not revealed by gamma alone. For instance, irrational orientations or high-index planes 10°–20° {111} have a high fraction of six- or sevenfold coordinated atoms. The importance of six- to sevenfold coordination on dissolution may be greater than the static composite value of gamma. The root cause of dissolution differences with orientation not only needs to consider atomic structure but also needs to consider the effect of Cl^- adsorption.[25] Cl^- adsorption is the next step to be considered.

Both thermodynamic and kinetic arguments can be made from these results. In this study, both Pd and Fe dissolve and the system is far from equilibrium. Therefore, the main effect of thermodynamics is rationalized to be its influence the oxidation overpotential and resulting charge transfer oxidation kinetics. Let us consider a single pure element. The change in Gibb's free energy, ΔG, can be rewritten in terms of the chemical potential, μ, and the reduced state can be modified to include the surface energy, γ:

$$\Delta G(\gamma) = G_{\text{oxidized}} - G_{\text{reduced}} = \sum \upsilon\mu_{\text{oxid}} - \sum \upsilon(\mu_{\text{red}} - k\gamma), \quad (2)$$

where ν is the stoichiometric coefficient and k is a correction factor. This equation can be used to calculate the electrochemical half-cell potential expressed as a reduction potential, E^0, as a function of surface energy of a specific $\{hkl\}$ as follows:

$$\Delta G(\gamma) = -nFE^0, \quad (3)$$

$$E^0 = \frac{\sum \upsilon\mu_{\text{oxid}} - \sum \upsilon(\mu_{\text{red}} - k\gamma_{\{hkl\}})}{nF}, \quad (4)$$

where the number of electrons transferred is n and F is Faraday's constant. The E^0 value for a specific $\{hkl\}$ determines η, the overpotential, and thereby the driving force for electrochemically controlled dissolution at an applied potential of $0.45V_{\text{SCE}}$.

$$E_{\text{app}}\,(0.45\ V_{\text{SCE}}) - E^0_{\{hkl\}} = \eta_{\{hkl\}}. \quad (5)$$

A grain orientation with high surface energy would lead to a more negative Nernst potential and at the $0.45V_{\text{SCE}}$ applied potential a faster dissolution rate. The difference between the maximum and minimum {hkl} in surface energy calculations of FCC metals ranged from 0.1 to 0.6 J/m^2,[17] assuming an atomic density of 1.4×10^{15} atoms/cm^2. Our calculations show that the difference between the highest and lowest energy grains for FePd falls at the lower end of the spectrum of maximum difference in surface energies at about 0.13 J/m^2.

Using this value in surface energy calculations, the difference in E^0 between different orientations can be approximated using Eq. (4). In this case, η is about 0.032 V higher. This would increase the oxidation current density [Eq. (6)] threefold for those high-energy orientations relative to lower energy orientations for a given Tafel slope, b_a.

$$i = i_0 10^{\Delta\eta/b_a}. \quad (6)$$

The exchange current density, i_0, also likely changes based on surface energy considerations [$i_0 \propto \exp(-\Delta G/\text{RT})$]. The adsorption of Cl^- is a likely reaction step in multi-step dissolution processes and likely produces further modified orientation dependence. Given these effects, the irrational facets may be expected to dissolve up to an order of magnitude faster assuming an anodic Tafel slope of 30–60 mV and charge transfer controlled kinetics.

Terrace and ledge structure

The morphology of post-exposure grains is dominated by microscopic terraces and ledges. Grains with orientations near {100} and {111} have the scalloped-like structure with no apparent terraces or ledges and grains exhibit the lowest surface roughness even after increased dissolution. Grains at higher $\beta_{\{100\}}$ (and $\beta_{\{111\}}$ >10°) have micrometer scale structural features dominated by terraces and ledges. For instance, grain 2 after increased dissolution [Figs. 1(a)–1(c)] are good examples of highly dissolved, high crystallographic surface roughness grains, which develop a corrosion-induced characteristic faceted structure. After increased dissolution the micrometer scale faceted structure becomes more pronounced [Fig. 1(e)]. These results are consistent with the published results for fcc Al where high-index orientations dissolve to form {111} and {100} terraces and the {111} terraces dissolve in a ⟨110⟩-direction.[3]

Grains with the highest surface roughness show similar characteristic crystallographic features. These grains also have the highest dissolution rate. As the fcc FePd grain orientation diverges from the {100} orientation, micrometer scale ledges become increasingly prevalent. Comparisons of grains 1, 3, and 5 which have increasing $\beta_{\{100\}}$ from 9.1° to 17.1° to 21.1°, respectively, reveal this feature. This correlation supports the idea that the crystallographic faceting of a given grain orientation is predominantly determined by the dissolution rate of the slowly dissolving low-index terraces and the fast lateral (Lateral with respect to the terrace, often not the original surface orientation.) dissolution of the likely higher index ledges. After increased dissolution, the structural features become even more apparent [Fig. 1(e)]. This {533} grain falls within orientation range of highest dissolution. Thus, the large surface area of highly dissolving facets leads to the overall high dissolution susceptibility and distinct facet structure. As in the case of crystal growth, fast-growing crystallography planes grow out of existence.[22] In this case, the dissolution rate slows down when fast-dissolving irrational facets dissolve out of existence to reveal an array of slow-dissolving low-index planes.

This grain behavior is consistent with the mechanistic interpretation of these results; the overall dissolution rate is determined by type and fraction of surface coverage of steps and

https://doi.org/10.1557/mrc.2014.23 Published online by Cambridge University Press

terraces. At the atomic level, these irrational planes possess a higher density of surface atoms with low coordination.

Conclusions

Disordered fcc FePd undergoes crystallographic-dependent dissolution during polarization well above reversible electrode potentials in HCl solution and develops low-energy crystal facets. The dissolution depth after a given time was found to depend on the crystal plane of the exposed surface. Of the 300 orientations measured, the {100} and {111} orientations were found to be the most dissolution resistant. The most corrosion susceptible region was between 10° and 20° from the {111} plane normal. Dissolution increased linearly as a function of the angle between the plane normal and the pole normal up to 40° from the {100} plane normal and up to 10° from the {111} plane normal. The increase in dissolution with crystallographic angle from the {100} orientation was substantially lower than from the {111} orientation.

The corrosion-induced micrometer scale crystallographic surface faceted structure was found to correlate with {*hkl*} dissolution depth. The surface faceting and corresponding roughness were greatest in regions of highest dissolution, whereas orientations near the {100} and {111} planes remained relatively smoother. During dissolution the crystallographic terrace–ledge faceted structure was maintained in individual grains after increased dissolution. These observations are consistent with dissolution eventually revealing slow dissolving low-index terraces and steps, and further dissolution proceeding most rapidly laterally on irrational ledge and kink facets. A comparison to surface energy revealed similar trends, but an exact correlation was not confirmed likely due to the effects of the orientation-dependent Cl^- adsorption.

Acknowledgments

This work was supported by the National Science Foundation under grant numbers DMR-0504983 and DMR-0906663 with Dr. Alen J. Ardell as a contract monitor. Professors W.A. Soffa and W.A. Jesser are thanked for materials and for extremely helpful discussions.

References

1. K. Fushimi, K. Miyamoto, and H. Konno: Anisotropic corrosion of iron in pH 1 sulphuric acid. *Electrochim. Acta* **55**, 7322 (2010).
2. B. Holme, N. Ljones, A. Bakken, O. Lunder, J.E. Lein, L. Vines, T. Hauge, O. Bauger, and K. Nisancioglu: Preferential grain etching of AlMgSi(Zn) model alloys. *J. Electrochem. Soc* **157**, C424 (2010).
3. E.V. Koroleva, G.E. Thompson, P. Skeldon, and B. Noble: Crystallographic dissolution of high purity aluminium. *Proc. R. Soc. A* **463**, 1729 (2007).
4. R.S. Lillard, G.F. Wang, and M.I. Baskes: The role of metallic bonding in the crystallographic pitting of magnesium. *J. Electrochem. Soc.* **153**, B358 (2006).
5. M. Sugiyama, S. Harada, and R. Oshima: Change in Young modulus of thermoelastic martensite Fe-Pd alloys. *Scr. Metall. Mater.* **19**, 315 (1985).
6. B.W. Davis, P.J. Moran, and P.M. Natishan: Metastable pitting behavior of aluminum single crystals. *Corros. Sci.* **42**, 2187 (2000).
7. A. Schreiber, J.W. Schultze, M.M. Lohrengel, F. Karman, and E. Kalman: Grain dependent electrochemical investigations on pure iron in acetate buffer pH 6.0. *Electrochim. Acta* **51**, 2625 (2006).
8. A. Shahryari, J.A. Szpunar, and S. Orrianovic: The influence of crystallographic orientation distribution on 316LVM stainless steel pitting behavior. *Corros. Sci.* **51**, 677 (2009).
9. G.M. Treacy and C.B. Breslin: Electrochemical studies on single-crystal aluminium surfaces. *Electrochim. Acta* **43**, 1715 (1998).
10. M. Yasuda, F. Weinberg, and D. Tromans: Pitting corrosion of Al and Al–Cu single-crystals. *J. Electrochem. Soc* **137**, 3708 (1990).
11. M. Gentile, E.V. Koroleva, P. Skeldon, G.E. Thompson, P. Bailey, and T.C. Q. Noakes: Influence of grain orientation on zinc enrichment and surface morphology of an Al-Zn alloy. *Surf. Interface Anal.* **42**, 287 (2010).
12. U. Konig and B. Davepon: Microstructure of polycrystalline Ti and its microelectrochemical properties by means of electron-backscattering diffraction (EBSD). *Electrochim. Acta* **47**, 149 (2001).
13. K.A. Lill: *Electrochemical Investigations on the Corrosion Properties of New Classes of Lightweight Steels, in Chemistry* (Max-Planck-Institut für Eisenforschung, Düsseldorf, 2008), p. 123.
14. H.J. Bunge: *Texture Analysis in Materials Science: Mathematical Methods*, English ed. (Butterworths, London, Boston, 1982).
15. C.E. Santo, E.W. Lam, C.G. Elowsky, D. Quaranta, D.W. Domaille, C. J. Chang, and G. Grass: Bacterial killing by dry metallic copper surfaces. *Appl. Environ. Microbiol.* **77**, 794 (2011).
16. G. Grochola, S.P. Russo, I. Yarovsky, and I.K. Snook: "Exact" surface free energies of iron surfaces using a modified embedded atom method potential and lambda integration. *J. Chem. Phys.* **120**, 3425 (2004).
17. J.-M. Zhang, F. Ma, and K.-W. Xu: Calculation of the surface energy of FCC metals with modified embedded-atom method. *Appl. Surf. Sci.* **229**, 34 (2004).
18. M.M. Lohrengel, A. Schreiber, and C. Rosenkranz: Grain-dependent anodic dissolution of iron. *Electrochim. Acta* **52**, 7738 (2007).
19. J.K. Mackenzie, A.J.W. Moore, and J.F. Nicholas: Bonds broken at atomically flat crystal surfaces—I: face-centred and body-centred cubic crystals. *J. Phys. Chem. Solids* **23**, 185 (1962).
20. J. Nicholas: Calculation of surface energy as a function of orientation for cubic crystals. *Austr. J. Phys.* **21**, 21 (1968).
21. M.B. Ives: On kink kinetics in crystal dissolution. *J. Phys. Chem. Solids* **24**, 275 (1963).
22. J.M. Howe: *Interfaces in Materials: Atomic Structure, Thermodynamics and Kinetics of Solid-vapor, Solid-liquid and Solid-solid Interfaces* (Wiley, New York, 1997).
23. J.C. Heyraud and J.J. Metois: Equilibrium shape and temperature—lead on graphite. *Surf. Sci.* **128**, 334 (1983).
24. M. McLean: Determination of the surface energy of copper as a function of crystallographic orientation and temperature. *Acta Metall. Mater.* **19**, 387 (1971).
25. G. Valette, A. Hamelin, and R. Parsons: Specific adsorption on silver single-crystals in aqueous-solutions. *Z. Phys. Chem. Neue. Fol.* **113**, 71 (1978).

https://doi.org/10.1557/mrc.2014.23 Published online by Cambridge University Press